Non-contact biomedical photoacoustic and ultrasound imaging

Guy Rousseau
Bruno Gauthier
Alain Blouin
Jean-Pierre Monchalin

Non-contact biomedical photoacoustic and ultrasound imaging

Guy Rousseau, Bruno Gauthier, Alain Blouin, and Jean-Pierre Monchalin
Industrial Materials Institute, National Research Council of Canada, 75 De Mortagne Boulevard, Boucherville, Québec J4B 6Y4, Canada

Abstract. The detection of ultrasound in photoacoustic tomography (PAT) usually relies on ultrasonic transducers in contact with the biological tissue through a coupling medium. This is a major drawback for important potential applications such as surgery. Here we report the use of a remote optical method, derived from industrial laser-ultrasonics, to detect ultrasound in tissues. This approach enables non-contact PAT (NCPAT) without exceeding laser exposure safety limits. The sensitivity of the method is based on the use of suitably shaped detection laser pulses and a confocal Fabry-Perot interferometer in differential configuration. Reliable image reconstruction is obtained by measuring remotely the surface profile of the tissue with an optical coherence tomography system. The proposed method also allows non-contact ultrasound imaging (US) by applying a second reconstruction algorithm to the data acquired for NCPAT. Endogenous and exogenous inclusions exhibiting optical and acoustic contrasts were detected *ex vivo* in chicken breast and calf brain specimens. Inclusions down to 0.3 mm in size were detected at depths exceeding 1 cm. The method could expand the scope of photoacoustic and US to *in-vivo* biomedical applications where contact is impractical. © *2012 Society of Photo-Optical Instrumentation Engineers (SPIE).* [DOI: 10.1117/1.JBO.17.6.061217]

Keywords: photoacoustic tomography; photoacoustic imaging; ultrasound imaging; optical detection of ultrasound; optical coherence tomography; brain surgery; blood oxygenation.

Paper 11509SS received Sep. 15, 2011; revised manuscript received Feb. 6, 2012; accepted for publication Feb. 27, 2012; published online May 7, 2012.

1 Introduction

Photoacoustic tomography (PAT),[1–3] which provides images of the optical absorption contrast, holds promise for many biomedical applications while ultrasound imaging (US) is a well established modality based on acoustic contrast of tissues. Both PAT and US usually rely on ultrasonic transducers in contact with the tissue using a coupling fluid (water or gel). Unfortunately, a physical contact is not suitable for many potential applications such as brain surgery.[4] Most extracorporeal applications are compatible with the use of a coupling fluid but some, such as burn diagnostic, are not. In ophthalmology, measurements of the retina properties will certainly benefit from non-contact detection on the retina itself or on other inaccessible layers within the eye.[5] For small animal imaging[6] and photoacoustic microscopy,[7,8] immersion in water can be awkward. Consequently, non-contact optical detection of ultrasound in biological tissues is of great interest. Moreover, generation and detection of ultrasound by remote optical means could facilitate endoscopic implementations of PAT and US as well as compatibility with other imaging modalities such as optical coherence tomography (OCT) for multimodal implementations.[9] Air-coupled transducers[10] have been considered for non-contact PAT, but their limited sensitivity could be difficult to overcome, especially when spatial resolution is needed. Attempts have been made to replace piezoelectric transducers by optical means, but most of these attempts still require contact with the tissue or immersion in water.[9,11–14] Most non-contact

strategies[11,14] need a liquid overlayer (water or oil) in order to reach an acceptable sensitivity by using the specular reflection of the air-liquid interface, which also implies a careful alignment, instead of using the diffuse reflection occurring on the natural surface of biological tissues.

Laser-ultrasonics[15] (LU) is a well-established optical technique allowing non-contact generation and detection of ultrasound. LU is mostly applied to industrial materials such as metals, plastics, and polymer-matrix composites. Ultrasound is laser generated by thermoelastic expansion or by ablation at the surface of the material and ultrasonic reflections coming back to the surface are detected using a laser beam reflected/backscattered on the material. The reflected/backscattered light, which is phase modulated by the surface displacement, is demodulated with a large etendue interferometer such as a confocal Fabry-Perot interferometer[16,17] (CFPI) or a photorefractive interferometer (PRI).[18,19] The sensitivity is given by the minimum measurable ultrasonic surface displacement. High sensitivity is obtained by using a high-power detection laser and operating in a shot-noise-limited detection regime. The challenge in applying to biomedical imaging the optical detection scheme used in LU consists in obtaining an acceptable sensitivity without exceeding laser exposure safety limits.[20] Non-contact PAT has been first demonstrated on industrial materials,[21] for which there is essentially no safety limit issue, and we have very recently reported the feasibility on biological tissue.[22]

In this work, which is a continuation of our recently published developments,[22] the optical detection scheme used in industrial LU is adapted to the safe detection of ultrasound in biological tissue. The technique does not require any contact,

Address all correspondence to: Guy Rousseau, Industrial Materials Institute, National Research Council of Canada, 75 De Mortagne Boulevard, Boucherville, Québec, J4B 6Y4, Canada. Tel: 450-641-5440; Fax: 450-641-5106; E-mail: guy.rousseau@cnrc-nrc.gc.ca

coupling medium, or surface preparation. Non-contact PAT (NCPAT) is implemented using a safe level of laser radiation by limiting the duration of high-energy detection laser pulses to the propagation time of ultrasound. A quantum-limited sensitivity is obtained using a differential optical phase demodulator. Instead of using a slow *z*-scan procedure to measure remotely the surface profile as in a previous work,[22] a time-domain OCT system[23] is used in this work to reduce the uncertainty about the surface position, thus allowing higher-resolution NCPAT imaging. A direct by-product of the NCPAT approach is the non-contact US (NCUS) obtained by applying a second reconstruction algorithm to the same data. The approach described herein is thus intrinsically bimodal, allowing the safe detection of inclusions exhibiting optical and acoustic contrasts. Inclusions down to 0.3 mm in size located at depths exceeding 1 cm were detected *ex vivo* in chicken-breast specimens. Promising preliminary results have also been obtained *ex vivo* with calf brain specimens. The technique is expected to be applicable *in vivo*.

2 Systems and Methods

The description of systems and methods presented below is similar to that recently published[22] and is reproduced here for the sake of completeness, but several modifications and additions have been included.

2.1 Shaping of the Detection Laser Pulses

Using laser beams to generate and detect ultrasound in biological tissues immediately leads to opposite requirements. First, the sensitivity of the measurement can only be increased by using a higher power of laser radiation. Second, the laser power is limited by safety limits; namely, the maximum permissible exposure (MPE), to avoid damaging the biological tissue.[20] Those opposite requirements necessitate an appropriate laser exposure management.

Efficient laser generation of acoustic waves is obtained with sufficiently short laser pulses compared with thermal and stress relaxation times.[3] Typically, few nanosecond pulses produced by Q-switched lasers are appropriate. In practice, the tissue is exposed repetitively over a large surface area, and the average intensity is limited by the MPE for a repetitive laser exposure.[20]

The power management is mostly related to the detection laser. When probing soft tissues at depths limited to 1 or 2 cm, propagation delays of ultrasonic waves are below 20 μs since the propagation velocity is about 1.5 mm/μs. The detection laser illumination should thus be limited to the propagation delay to minimize laser exposure. For most industrial applications, a master oscillator (MO) power amplifier emitting powerful long pulses is appropriate. Such a laser source can be adapted to biomedical applications by limiting the pulse duration without losing energy in the laser system. This is done by adding an intensity modulator (IMOD) between the continuous wave (cw) MO and the power amplifier. A schematic diagram of such a laser source is shown in Fig. 1(a). The IMOD allows inhibiting the amplifier output at the beginning of each pumping flash by setting its transmission to zero. The energy then builds up in the amplifier laser rods (LRs). Before the end of each pumping flash, the IMOD transmission is increased gradually to release the stored energy and obtain the desired pulse duration and shape at the amplifier output. Without pulse shaping [dashed line in Fig. 1(b)], the laser pulse has an energy of 35 mJ, a peak power of 280 W, and a duration
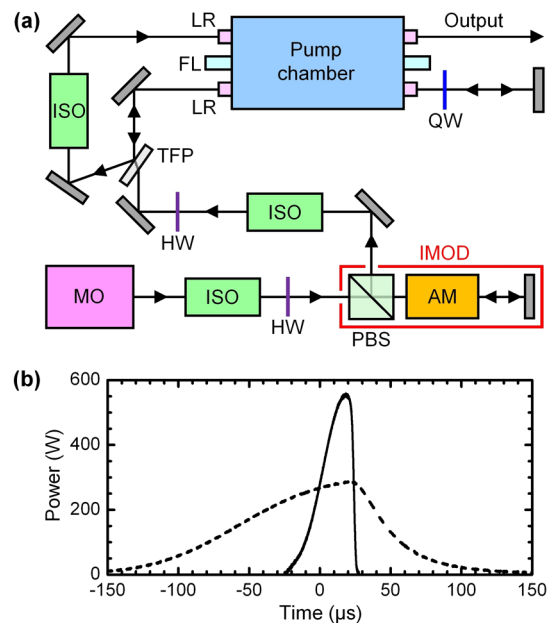

Fig. 1 Detection laser. (a) Layout of the system. MO, Nd:YAG cw master oscillator; ISO, optical isolator; HW, half-wave plate; PBS, polarizing beam splitter; AM, amplitude modulator; IMOD, intensity modulator; TFP, thin-film polarizer; LR, Nd:YAG laser rod; FL, flashlamp; QW, quarter-wave plate. Other components are plane dielectric mirrors. (b) Natural pulse shape of the detection laser (dashed line) and tailored pulse shape (solid line) used in the experiment. The generation laser pulse occurs at $t = 0$ μs.

of 110 μs (FWHM: full width at half maximum). With pulse shaping [solid line in Fig. 1(b)], the laser pulse tailored for this experiment has an energy of 14 mJ, a peak power of 560 W, and a duration of 24 μs (FWHM). Reducing the pulse duration thus increases the available peak power. More importantly, the peak power for a given energy is about five times higher with the tailored pulse. The tailored pulse was shaped with an increasing instantaneous power for two reasons. First, this eliminates strong signal oscillations at the output of high-pass filters preceding signal digitization. Second, the sensitivity increases with time to facilitate the detection of weaker signals arriving at larger time delays (coming from larger depths in the tissue).

2.2 Scanning and Detection Systems

A schematic diagram of the scanning setup is shown in Fig. 2(a). The generation laser (not shown) is a Q-switched laser emitting 5 ns pulses at 532 nm with a repetition frequency of 10 Hz. The generation laser beam is directed toward the biological tissue specimen after beam expansion and transmission through a line mask, blocking the generation laser on the detection scan line. The detection laser beam is transmitted to the setup by a multimode optical fiber. A sample of the detection laser beam is first deflected by a beam splitter (BS) and coupled into an optical fiber as a reference beam for phase-noise elimination. The detection laser beam is then focused on a 400-μm-diameter spot on the tissue specimen. A small prism mirror (*P*) in front of the collecting optics is used to direct the detection beam to the tissue without coupling stray light into the collecting optics. The resulting illumination/detection geometry is shown
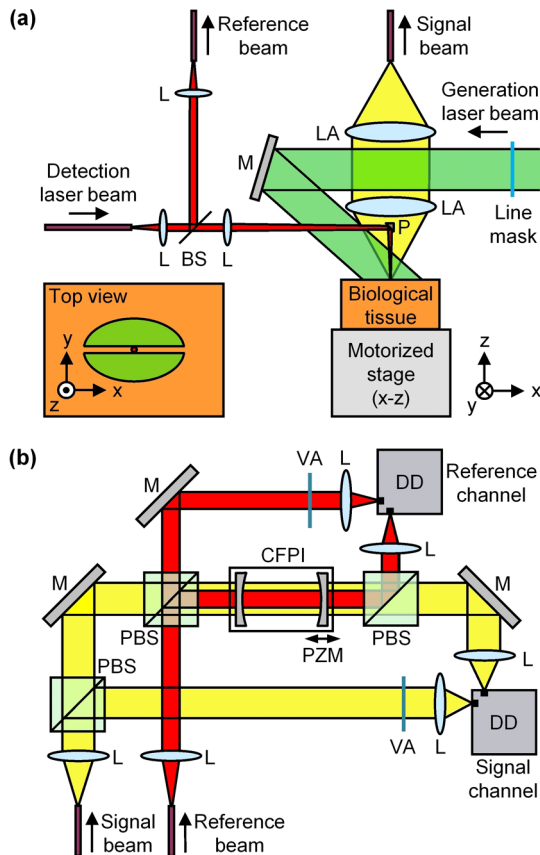
Fig. 2 Experimental setup. (a) Schematic diagram of the biological tissue scanning setup. LA, lens assembly; L, lens; M, plane mirror; BS, beam splitter; P, gold coated hypotenuse prism. (b) Schematic diagram of the CFPI in differential configuration. PBS, polarizing beam splitter; PZM, piezoelectrically actuated mirror mount; VA, variable attenuator; DD, differential detector.

in the inset [Fig. 2(a)] where the elliptic area is the generation laser spot (masked on the scan line), and the centered circular area is the detection laser spot. The line mask eliminates any overlap between illumination and detection, thus allowing an independent evaluation of the MPE for generation and detection lasers. The collecting optical system uses two lens assemblies (LAs) for collimating and coupling the reflected/backscattered light into the signal beam optical fiber (400-μm-core diameter, 0.39 numerical aperture). The biological tissue specimen is located on a computer-controlled motorized stage, allowing displacements along the scanning axis x and the focusing axis z.

The phase demodulation of the collected light is done with an actively stabilized CFPI mounted in differential configuration to achieve both intensity and phase-noise reduction [Fig. 2(b)].[24] The horizontal polarization is used to demodulate light from the tissue specimen (signal beam), and the vertical polarization is used to measure the phase noise of the detection laser (reference beam). A CFPI has been preferred to a PRI since a PRI needs a longer illumination of the biological tissue to write the adaptive volume grating inside the photorefractive crystal. This longer illumination implies that more energy is delivered to the tissue for a given peak power. Although this is not critical for material,[21] the shortest illumination time is preferable in biomedical applications where the exposure is limited by safety limits.[20] The CFPI is a 1-m-long cavity with mirrors' reflectivity

of 94.5%. The back mirror is mounted on a piezoelectrically actuated mount (PZM) fed by a servo loop ensuring stabilization at half-maximum of the carrier frequency transmission. This provides a peak demodulation response at about 2 MHz with an acceptable response (larger than 30% of the peak) between 400 kHz and 9 MHz.[17,22] For both reference and signal beams, a differential detector (DD) is used for intensity noise reduction. Each DD uses two InGaAs photodiodes in series DC-coupled to a transimpedance amplifier followed by a high-pass filter (300-kHz cutoff frequency) and a voltage amplifier. Reference and signal channels are digitized and processed to eliminate the phase noise of the laser source by the adaptive filtering explained as follows. First, the amplitude of the signal channel before the generation laser pulse was multiplied to obtain an rms noise equal to that of the reference channel in the same time window. Then iterations around this first value have allowed determining the optimum amplitude multiplication factor to minimize the residual noise on the difference between both channels. Typically, the residual noise was comparable with the shot noise level calculated from nominal values of the transimpedance gain and InGaAs photodiodes' quantum efficiency. The spectrum of the residual noise was practically white in the frequency range kept for the analysis (0.5 to 3 MHz). The adaptive filter also included a fixed numerical delay between both channels to account for any electronic delay in the setup.

2.3 Image Reconstruction

A typical image is obtained from 60 to 80 A-scans, each measured with a single detection laser pulse (no averaging). All A-scans are grouped in a raw B-scan image, which is processed with the synthetic aperture focusing technique (SAFT).[3,25] The SAFT algorithm is applied in the time domain and takes into account the surface profile of the biological tissue. When measuring remotely on curved surfaces with non-negligible height variations compared with the minimum ultrasonic wavelength (about 0.5 mm at 3 MHz), the surface profile is an essential input for a reliable image reconstruction. In the experiment described here, unlike in the one previously reported, in which the z-scan approach was used,[22] the surface profile was measured prior to the scan with an OCT system. Each raw B-scan image, once linked with the surface profile, contains all the necessary information for both NCPAT and NCUS imaging modes. This is due to two concomitant ways of generating ultrasound in the specimen. When the generation laser pulse illuminates the specimen, a significant proportion of the incoming light is diffusely reflected. This light penetrates only at shallow depths and is lost in free space after a few scattering events. The remaining light penetrates more deeply in the specimen by following highly randomized optical paths. The fluence associated to these penetrating photons decreases rapidly with depth.[3]

Light penetrating more deeply into the specimen contributes essentially to the photoacoustic generation on optical absorbers (e.g., blood vessels), the strength of the thermoelastic generation occurring on each absorber being related to the product of the local laser fluence, and its absorption coefficient at the generation laser wavelength (GLW). Ultrasonic waves generated in this process then propagate up to the surface of the tissue where they can be detected. The only difference with conventional PAT is the non-contact optical detection and the fact that the surface profile must be taken into account in the reconstruction,

which is not generally needed in conventional PAT due to the known position of transducer(s) and the close acoustic impedances of water and tissue.

The high laser fluence present at shallow depths contributes to the thermoelastic generation of an ultrasonic wave at the surface (or close to it) by the background absorption of the tissue. Even though the background absorption is usually low (when the GLW is properly chosen), the product of the high laser fluence at low depth with the low background absorption of the tissue is usually sufficient to generate an acoustic waves in a similar manner to industrial LU where the penetration depth of photons is usually much shorter. The ultrasonic wave generated by this process has an initial area equal to that of the generation laser spot and a wavefront following essentially the surface topography of the specimen over this area. This ultrasonic wave then propagates inside the tissue, and any acoustic impedance mismatch will reflect or backscatter ultrasonic waves toward the surface were they can be detected.

Consequently, the same data can be used for both NCPAT and NCUS, the only difference being the propagation delay, as schematically shown in Fig. 3. In the case of NCPAT [Fig. 3(a)], the delay is the propagation time from the absorbing inclusion to the detection location at the surface. In the case of NCUS [Fig. 3(b)], the delay includes, in addition, the propagation time from the surface to the acoustically mismatched inclusion.

The relative strength of both generation processes depends on the tissue optical properties and the chosen GLW. If the background absorption of the tissue is strong at the GLW, the ultrasonic wave generated at the surface will be strong, and less light will be available for photoacoustic generation at absorbing sites inside the tissue. On the contrary, if the background absorption of the tissue is very low at the GLW, the thermoelastic generation at the surface will be very low and more light will be available inside the specimen for thermoelastic generation on optical absorbers. In general, both generation processes will occur concomitantly. Of course, if the choice of the GLW strongly favors one mode of generation, this will be detrimental to the other. Most of the time, however, the technique is intrinsically bimodal; the same data being used for both processed images. The only difference is the expression for the temporal delay: the one-way propagation delay is used for NCPAT reconstruction, and the two-way propagation delay is used for NCUS reconstruction. When used as a bimodal technique, the photoacoustic signals may lead to artifacts in the NCUS image and the ultrasonic

signals may lead to artifacts in the NCPAT image. However, these artifacts will generally be faint since SAFT reconstruction will not properly focus signal of one mode into the other one. More advance processing may also be used to minimize these artifacts, which can be seen as a kind of crosstalk.

The algorithm used for image reconstruction was time-domain SAFT. After applying adaptive filtering for noise reduction, each A-scan was numerically filtered with a third-order Bessel-type bandpass filter using typical cutoff frequencies of 0.5 and 3 MHz. With a lateral step size of 400 μm, using frequencies higher than 3 MHz only increases the background noise without a significant gain in spatial resolution.[26] Each A-scan was delayed according to the measured surface profile and to the speed of sound in the specimen (typically 1.55 mm/μs). The reconstruction grid included interpolation along the axis x to reduce the lateral pixel size to 100 μm instead of the experimental lateral step of 400 μm. The vertical size of the pixel was set to 100 μm in the reconstruction. Consequently, processed images were obtained with a pixel size of 100×100 μm^2. For both imaging mode, the time derivative of each A-scan was used to account for the fact that pressure is proportional to the velocity of the surface, not to its displacement.[21] Although this is an approximate procedure, image quality was found to be improved in this way. Taking the true frequency response of a CFPI would be more accurate.[17,22]

In the present work, the OCT measurements were performed prior to the scan but the working distance of the OCT system was similar to that of our setup (25 mm). Consequently, both systems could be integrated using a dichroic mirror. In this first implementation, a B-scan of 80 A-scans can be measured in 8 s. The processing time for NCPAT and NCUS was below 1 s. Consequently, measurement and processing time below 10 s is achievable without exceeding MPE for results shown in the following section.

2.4 Preparation of Tissues and Exogenous Inclusions

Chicken breasts were cut parallel to the natural surface to obtain a uniform thickness of about 10 mm for the upper part of the breast. This procedure was used to ensure that the natural surface of the upper piece was intact (without any incisions or preparation) for laser measurements. In the lower piece of the breast, 1- to 2-mm-deep incisions were made with a scalpel and gently filled with vegetable oil using a syringe before inserting exogenous inclusions described below. Vegetable oil was also poured between both pieces of chicken breast for a better ultrasonic contact when the upper piece was put back over the lower piece. Calf brains were prepared similarly, thus keeping intact the natural upper surface of the brain for laser probing.

Blood vessels were simulated with polyester thin wall tubes filled with India ink diluted to obtain an absorption coefficient μ_a comparable with that of whole blood at 532 nm, which is about 235 cm^{-1} for oxyhemoglobin and 217 cm^{-1} for deoxyhemoglobin. Those values were obtained by assuming a whole blood concentration of hemoglobin of 150 g Hb/l.[27] The polyester tubes were optically transparent at visible and near-infrared wavelengths and the nominal wall thickness was 12.7 μm. The negligible wall thickness compared with the shortest ultrasound wavelength considered in the experiment (about 0.5 mm) also ensured a good acoustic transparency. Consequently, these phantoms were appropriate to mimic the optical absorption of blood vessels while
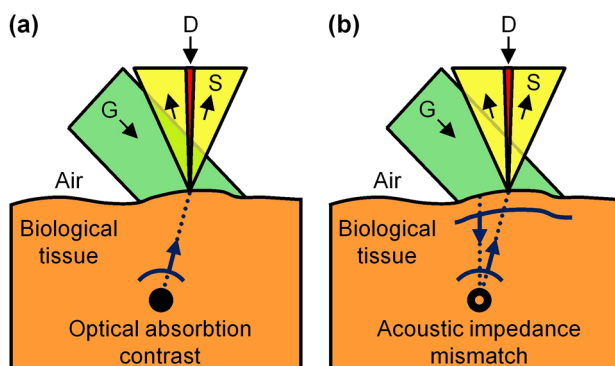

Fig. 3 Reconstruction methods. (a) One-way path used in NCPAT imaging mode. (b) Two-way path used in NCUS imaging mode. G, generation laser beam; D, detection laser beam; S, signal beam.

minimizing the ultrasonic impedance mismatch with the surrounding tissue.

Grayish metal wires were also used as exogenous inclusions to provide a strong ultrasonic impedance mismatch with the surrounding tissue. When used without white paint, their grayish color also ensured some optical absorption (to generate a photoacoustic signal). When painted white, their optical absorption was essentially eliminated, and no photoacoustic signal was expected in this case.

2.5 Laser Safety Limits and Sensitivity

For the generation laser, the average intensity must be considered since there is a significant overlap of the surface illuminated by the generation laser between successive points of the scan. The illuminated elliptic surface of 4.0 cm $\times$ 2.5 cm has an area of 7.9 cm^2. With 100 mJ pulses at 10 Hz, this corresponds to an average intensity of 130 mW/cm^2, well below the MPE at 532 nm (200 mW/cm^2).[20] The single-shot MPE, expressed in terms of fluence, can be used at the detection laser wavelength (1064 nm) since there is no overlap between successive points of the scan. Assuming a pulse duration t_p of about 25 μs, the MPE is given by $C_A\, t_p^{0.25} = 0.39$ J/cm^2 since $C_A = 5.0$ J/cm^2/s$^{0.25}$ at 1064 nm.[20] The 400-μm-diameter detection spot corresponds with a surface $S = 1.3 \times 10^{-3}$ cm^2. The maximum energy per pulse is thus $E_{max} = \text{MPE} \times S = 0.5$ mJ, which was the pulse energy used in the experiment.

The sensitivity can be estimated from the shot-noise limit, which was essentially reached after adaptive filtering. Considering the amount of light captured by detectors, we have estimated a noise equivalent pressure of 8 Pa for a bandwidth of 3 MHz (corresponding with a surface displacement of about 0.8 pm).[22] Some passive losses could be reduced further in our setup, but this first estimate gives the right order of magnitude. From the derivation performed in Ref. 28, we calculate a noise equivalent pressure of about 6 Pa for a 0.4-mm-diameter polyvinylidene fluoride (PVDF) transducer. Therefore, the sensitivity obtained during the experiment was comparable with the theoretical sensitivity of a piezoelectric transducer.[*]

3 Results

Measurements have been performed *ex vivo* on chicken breast and calf brain specimens. Different objects have been embedded into the specimens to demonstrate the sensitivity of the technique as well as the two reconstruction modes. In all cases, the detection spot diameter and the lateral step size were equal to 400 μm (no spatial oversampling). The frequency range used in the reconstruction was typically limited between 0.5 and 3 MHz.

3.1 Images of a Chicken Breast Specimen

Results obtained with a chicken breast specimen are shown in Fig. 4. As mentioned in Sec. 2.4, embedded objects were chosen to produce different combinations of photoacoustic and ultrasonic responses. The NCPAT image [Fig. 4(a)] and the NCUS image [Fig. 4(b)] of the same chicken breast specimen clearly exhibits the embedded objects zoomed below their respective image. The 0.7-mm-diameter grayish metal wire (*i*) is seen in
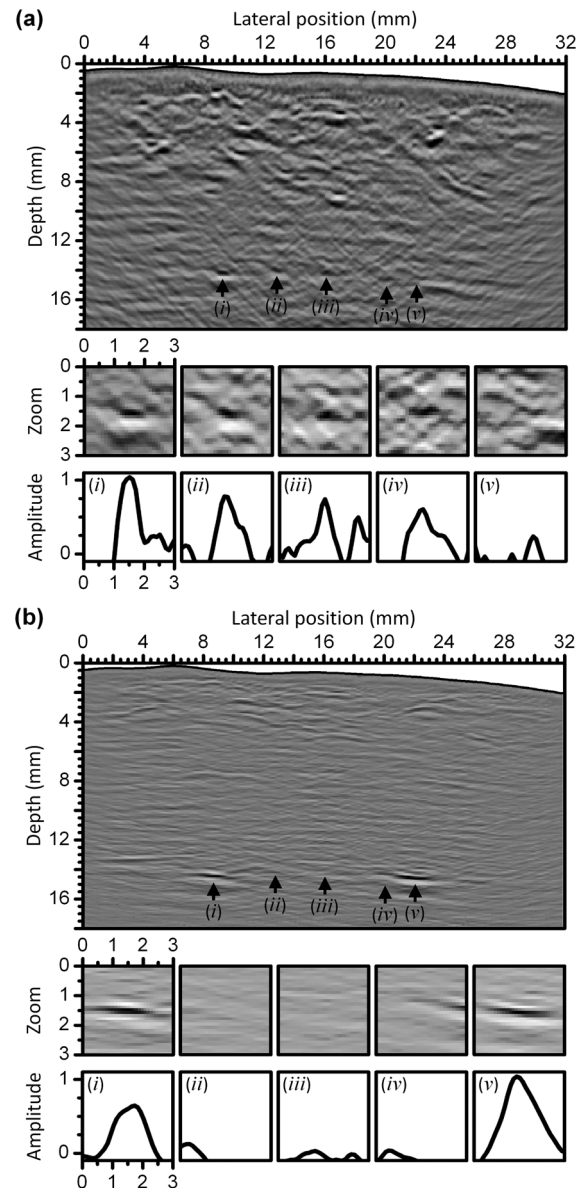

Fig. 4 Images of a chicken-breast specimen. (a) NCPAT image obtained with the following embedded objects (respective diameters in parenthesis): *i*, unpainted grayish metal wire (0.7 mm); *ii*, blood vessel phantom (0.5 mm); *iii*, blood vessel phantom (0.3 mm); *iv*, blood vessel phantom (0.7 mm); *v*, white painted metal wire (0.8 mm). (b) Corresponding NCUS image. All scales are in mm except for amplitude profiles (in arbitrary units).

both NCPAT and NCUS images. Blood vessel phantoms with diameters of 0.5 mm (*ii*), 0.3 mm (*iii*), and 0.7 mm (*vi*) are mainly seen in the NCPAT image. The 0.8-mm-diameter white-painted metal wire (*v*) is only seen in the NCUS image. Many additional dark spots seen in the NCPAT image are attributed to endogenous absorption sites. These darker spots should not be confused with noise spikes since successive measurements on the same chicken breast specimen gave reproducible results for both exogenous and endogenous absorption sites. Faint hyperbolic artifacts seen in Fig. 4(b), especially at shallow depths, are attributed to photoacoustic signals which are not properly focused by the NCUS reconstruction algorithm. The lateral amplitude profiles (along *x*) extracted for each embedded objects are also shown in Fig. 4 using the same

---

[*]In a previous publication (Ref. 22), we had omitted to take into account the difference of diameters between the PVDF transducer (5 mm in Ref. 28), which was estimated to have a noise equivalent pressure of about 0.5 Pa, and our detection spot (0.4 mm). For a PVDF transducer of 0.4 mm diameter, the calculation gives a noise equivalent pressure of 6 Pa.

vertical scale to exhibit both the lateral resolution and the relative signal strength. For the NCUS reconstruction, a proper modeling of the source near the surface and the following acoustic wavefront propagation are likely to improve the resolution beyond what is observed in Fig. 4(b).

3.2 Images of a Calf Brain Specimen

Results obtained with a calf brain specimen are shown in Fig. 5. Similar embedded objects were used to test the imaging capability. Again, each embedded object is zoomed below the main NCPAT image [Fig. 5(a)] and NCUS image [Fig. 5(b)]. The corresponding horizontal profiles are also shown. As expected, the 0.8-mm-diameter white-painted metal wire (*i*) is only seen in the NCUS image while blood vessel phantoms with diameters of 0.7 mm (*ii*), 0.5 mm (*iii*), and 0.3 mm (*iv*) are only seen in
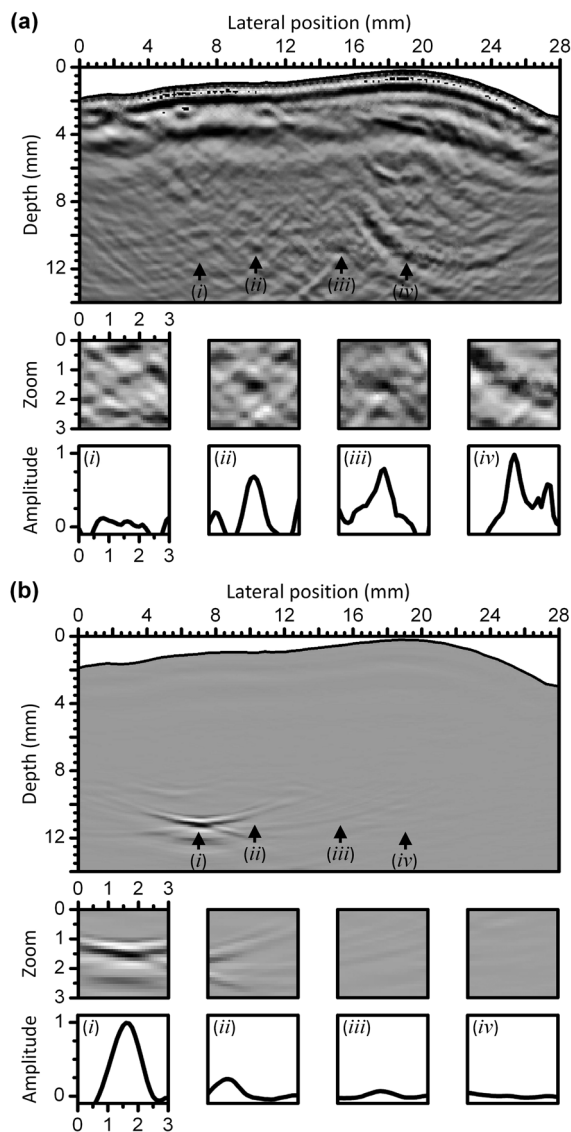

Fig. 5 Images of a calf brain specimen. (a) NCPAT image obtained with the following embedded objects (respective diameters in parenthesis): *i*, white-painted metal wire (0.8 mm); *ii*, blood vessel phantom (0.7 mm); *iii*, blood vessel phantom (0.5 mm); *iv*, blood vessel phantom (0.3 mm). (b) Corresponding NCUS image. All scales are in mm except for amplitude profiles (in arbitrary units).

the NCPAT image. In the NCUS image, the signal strength is good, but the lateral resolution is poor and is expected to be improved with better synthetic focusing obtained by using a three-dimensional (3-D) reconstruction algorithm, a two-dimensional (2-D) surface topography measurement, and the numerical modeling of the propagation of the generated ultrasonic wave. In this case, additional darker areas are also seen and may be first attributed to endogenous absorptions sites. However, due to the faster dehydration of the calf brain surface compared with the chicken breast surface, the reproducibility of results on calf brain was more difficult to verify. A validation method, such as x-ray computed tomography, would have been preferable, but this involves injecting a contrast agent in the blood prior to slaughtering the animal.

4 Discussion

The results presented herein give a clear demonstration of NCPAT and NCUS performed *ex vivo* on soft biological tissues. Sub-millimeter endogenous and exogenous inclusions have been detected at depths exceeding 1 cm. It is clearly shown that the highly scattering surface of a soft tissue provides a sufficiently strong diffused reflectivity to measure the ultrasonic displacement of the surface while remaining below the MPE. This, however, requires limiting the pulse duration of the detection laser to the propagation time of ultrasound. Using a differential configuration of the CFPI has also been essential to reach a quantum-limited sensitivity by removing both intensity and phase noise of the detection laser. For NCPAT imaging mode, the remote surface profile measurement was used to obtain a reliable image reconstruction using time-domain SAFT. Results obtained for the NCUS imaging mode were limited by the 2-D reconstruction algorithm and the 1-D surface profile measurement.

The present system was optimized for a 2-D reconstruction algorithm. Clearly, a 3-D reconstruction would be desirable for applications involving highly structured tissues such as brain. A 3-D algorithm would intrinsically increase the signal-to-noise ratio (SNR) by increasing the number of A-scans involved in the reconstruction of each point of the volume. This would allow to further reduce the detection laser energy and to superimpose generation and detection laser beams without reaching the MPE. Coupling this non-contact system with an OCT system would provide both a real-time measurement of the surface topography and the OCT image near the surface of the tissue, which is complementary with the present method. More fundamentally, the generation of the ultrasonic wave near the surface of the tissue and its propagation need to be modeled carefully in order to implement an NCUS reconstruction algorithm achieving a diffraction-limited resolution and sensitivity. An efficient NCUS mode must be based on a 3-D reconstruction algorithm and a 2-D surface topography measurement. Among possible applications, a multiwavelength version of the present system could provide a spatially resolved evaluation of blood oxygenation, which is critical in brain surgery for fast detection of ischemia. The need for a coupling medium being removed, a wealth of applications could also emerge from the present method.

References

1. P. Beard, "Biomedical photoacoustic imaging," *Interface Focus* **1**(1), 602–631 (2011).
2. L. V. Wang, Ed., *Photoacoustic Imaging and Spectroscopy*, CRC Press, Boca Raton, FL (2009).
3. L. V. Wang and H. Wu, *Biomedical Optics: Principles and Imaging*, John Wiley and Sons, Hoboken, NJ (2007).
4. V. Ntziachristos, J. S. Yoo, and G. M. van Dam, "Current concepts and future perspectives on surgical optical imaging in cancer," *J. Biomed. Opt.* **15**(6), 066024 (2010).
5. H. F. Zhang, C. A. Puliafito, and S. Jiao, "Photoacoustic ophthalmoscopy for in vivo retinal imaging: current status and prospects," *Ophthalmic Surg. Laser Imag.* **42**(4), S106–S115 (2011).
6. X. Wang et al., "Noninvasive laser-induced photoacoustic tomography for structural and functional in vivo imaging of the brain," *Nat. Biotech.* **21**(7), 803–806 (2003).
7. H. F. Zhang et al., "Functional photoacoustic microscopy for high-resolution and noninvasive in vivo imaging," *Nat. Biotech.* **24**(7), 848–851 (2006).
8. K. Maslov, G. Stoica, and L. V. Wang, "In vivo dark-field reflection-mode photoacoustic microscopy," *Opt. Lett.* **30**(6), 625–627 (2005).
9. E. Z. Zhang et al., "Multimodal photoacoustic and optical coherence tomography scanner using an all optical detection scheme for 3D morphological skin imaging," *Biomed. Opt. Express* **2**(8), 2202–2215 (2011).
10. R. G. M. Kolkman et al., "Feasibility of noncontact piezoelectric detection of photoacoustic signals in tissue-mimicking phantoms," *J. Biomed. Opt.* **15**(5), 055011 (2010).
11. B. P. Payne et al., "Optoacoustic tomography using time-resolved interferometric detection of surface displacement," *J. Biomed. Opt.* **8**(2), 273–280 (2003).
12. H. Grün et al., "Three-dimensional photoacoustic imaging using fiber-based line detectors," *J. Biomed. Opt.* **15**(2), 021306 (2010).
13. R. Nuster et al., "Downstream Fabry-Perot interferometer for acoustic wave monitoring in photoacoustic tomography," *Opt. Lett.* **36**(6), 981–983 (2011).
14. Y. Wang, C. Li, and R. K. Wang, "Noncontact photoacoustic imaging achieved by using a low-coherence interferometer as the acoustic detector," *Opt. Lett.* **36**(20), 3975–3977 (2011).
15. C. B. Scruby and L. E. Drain, *Laser-Ultrasonics: Techniques and Applications*, Adam Hilger, Bristol, UK (1990).
16. J.-P. Monchalin, "Optical detection of ultrasound at a distance using a confocal Fabry-Perot interferometer," *Appl. Phys. Lett.* **47**(1), 14–16 (1985).
17. J.-P. Monchalin, "Optical detection of ultrasound," *IEEE Trans. Ultrason. Ferroelectr. Freq. Control* **33**(5), 485–499 (1986).
18. R. K. Ing and J.-P. Monchalin, "Broadband optical detection of ultrasound by two-wave mixing in a photorefractive crystal," *Appl. Phys. Lett.* **59**(25), 3233–3235 (1991).
19. A. Blouin and J.-P. Monchalin, "Detection of ultrasonic motion of a scattering surface by two-wave mixing in a photorefractive GaAs crystal," *Appl. Phys. Lett.* **65**, 932–934 (1994).
20. American National Standard for the Safe Use of Lasers ANSI Z136.1-2007, Laser Institute of America, Orlando, FL (2007).
21. T. Berer et al., "Remote photoacoustic imaging on solid material using a two-wave mixing interferometer," *Opt. Lett.* **35**(24), 4151–4153 (2010).
22. G. Rousseau, A. Blouin, and J.-P. Monchalin, "Non-contact photoacoustic tomography and ultrasonography for tissue imaging," *Biomed. Opt. Express* **3**(1), 16–25 (2012).
23. G. Lamouche et al., "Optical delay line using rotating rhombic prisms," *Proc. SPIE* **6429**, 64292G (2007).
24. A. Blouin et al., "Differential confocal Fabry-Perot for the optical detection of ultrasound," in *Rev. Prog. in QNDE 26*, D. O. Thompson and D. E. Chimenti, Eds., pp. 193–200, Plenum, New York (2007).
25. J. Davies et al., "Review of synthetically focused guided wave imaging techniques with application to defect sizing," in *Rev. Prog. in QNDE 25*, D. O. Thompson and D. E. Chimenti, Eds., pp. 142–149, Plenum, New York (2006).
26. D. Lévesque et al., "Performance of laser-ultrasonic F-SAFT imaging," *Ultrasonics* **40**(10), 1057–1063 (2002).
27. S. Prahl, "Optical Absorption of Hemoglobin," Oregon Medical Laser Center. http://omlc.ogi.edu/spectra/hemoglobin/index.html.
28. A. A. Oraevsky et al., "Two-dimensional opto-acoustic tomography transducer array and image reconstruction algorithm," *Proc. SPIE* **3601**, 256–267 (1999).